Pressure-induced irreversible metallization accompanying the phase transitions in Sb$_2$S$_3$

Lidong Dai,[1,*] Kaixiang Liu,[1,2] Heping Li,[1] Lei Wu,[1] Haiying Hu,[1] Yukai Zhuang,[1,2] Linfei Yang,[1,2]
Chang Pu,[1,2] and Pengfei Liu[3]

[1]*Key Laboratory of High-Temperature and High-Pressure Study of the Earth's Interior, Institute of Geochemistry,*
Chinese Academy of Sciences, Guiyang, Guizhou 550081, China
[2]*University of Chinese Academy of Sciences, Beijing 100039, China*
[3]*State Key Laboratory of Structural Chemistry, Fujian Institute of Research on the Structure of Matter, Chinese Academy of Sciences,*
Fuzhou, Fujian 350002, China

We have revealed Sb$_2$S$_3$ to have two phase transitions and to undergo metallization using a diamond anvil cell at around 5.0, 15.0, and 34.0 GPa, respectively. These results were obtained on the basis of high-pressure Raman spectroscopy, temperature-dependent conductivity measurements, atomic force microscopy, high-resolution transmission electron microscopy, and first-principles calculations. The first phase transition at $\sim$5.0 GPa is an isostructural phase transition, which is manifested in noticeable changes in five Raman-active modes and the slope of the conductivity because of a change in the electronic structure. The second pressure-induced phase transition was characterized by a discontinuous change in the slope of conductivity and a new low-intensity Raman mode at $\sim$15.0 GPa. Furthermore, a semiconductor-to-metal transition was found at $\sim$34.0 GPa, which was accompanied by irreversible metallization, and it could be attributed to the permanently plastic deformation of the interlayer spacing. This high-pressure behavior of Sb$_2$S$_3$ will help us to understand the universal crystal structure evolution and electrical characteristics for A_2B_3-type compounds, and to facilitate their application in electronic devices.

I. INTRODUCTION

Antimony trisulfide (Sb$_2$S$_3$), a well-known binary semiconductor, belongs to the A_2B_3 family ($A =$ Bi, Sb, As; $B =$ S, Se, Te) of layered chalcogenide with an optical band-gap energy (E_g) of $\sim$1.7 eV [1]. This material has unique thermoelectric properties and can be exploited in a wide range of applications, such as optoelectronic devices, fuel cells, and gas sensors [2,3]. At ambient pressure, Sb$_2$S$_3$ crystallizes in a complex orthorhombic structure (SG *Pnma* No: 62, $Z = 4$, U$_2$S$_3$-type) [4]. This *Pnma* phase can be considered as a layered structure: stacking of SbS$_3$ and SbS$_5$ units yields a crumpled sheet-type disposition with infinite (Sb$_4$S$_6$)$_n$ units, resulting in layers extending mainly in the *b-c* plane and piled up mainly along the *a* axis [5].

As a representative layered chalcogenide semiconductor in the A_2B_3 series, Sb$_2$S$_3$ has attracted a lot of interest due to its exceptional thermoelectric property and technological applications [6,7]. Some crucial high-pressure characterizations of these A_2B_3-type compounds have been reported previously, such as structural phase transitions [8–10], electronic topological transitions (ETTs) [8–12], insulator-metal transitions [13], and superconductivity [13,14]. However, the structural and vibrational properties of Sb$_2$S$_3$ at high pressure remain controversial. In one study, an ETT phenomenon of Sb$_2$S$_3$ was observed by means of Raman spectroscopy and resistivity measurements near 5 GPa [15], along with a new

pressure-induced phase transition at $\sim$15 GPa [16]. In another study, which investigated the high-pressure crystal structure and cation lone-electron pair activity of Sb$_2$S$_3$ up to 10 GPa, one systematic stable crystal structure was found [17]. Pressure could suppress the lone-electron pair of Sb$_2$S$_3$, which may result in a structural phase transition and a change in the electronic properties. By contrast, Ibáññez *et al.* [5] recently observed that neither a pressure-induced ETT nor a second-order isostructural phase transition (IPT) occurs in Sb$_2$S$_3$ on the basis of synchrotron x-ray diffraction and Raman scattering data, as well as theoretical calculations.

It is well known that the ETT is an IPT without any volume discontinuity, and the Wyckoff positions of atoms are not modified during the transition. Measurement of high-pressure electrical transport is important for detecting the subtle changes that occur during an IPT. Furthermore, metallization of Sb$_2$S$_3$ at higher pressure is an unresolved problem. Sb$_2$Se$_3$, which has the same electronic structure as Sb$_2$S$_3$, undergoes a semiconductor-to-metal conversion at 3.5 GPa [13]. Although Sb$_2$S$_3$ has a wide-band-gap energy ($\sim$1.70 eV) at atmospheric pressure, pressure can be applied to tune the band gap and ultimately result in metallization. To the best of our knowledge, only one high-pressure electrical resistivity experiment has been reported up to $\sim$10 GPa for Sb$_2$S$_3$ [15], and theoretical calculations predict a semiconductor-to-metal transformation at $\sim$15 GPa [5]. Thus, further systematic investigation of the electrical properties at high pressure is required to determine whether metallization occurs for Sb$_2$S$_3$.

In the present study, we report two second-order IPTs and metallization for Sb$_2$S$_3$ at pressures up to $\sim$40.1 GPa using a

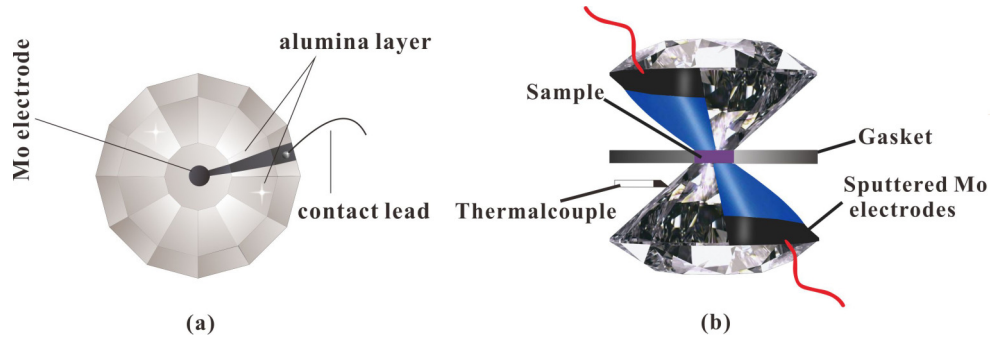*Corresponding author: dailidong@mail.gyig.ac.cn

FIG. 1. Experimental assembly for electrical conductivity measurement for Sb_2S_3. (a) Configuration of plate electrodes integrated between two symmetric diamond anvils. (b) Cross section of the DAC used for impedance spectroscopy measurement at high pressure.

diamond anvil cell (DAC) in conjunction with ac impedance spectroscopy, Raman spectroscopy, atomic force microscopy (AFM), high-resolution transmission electron microscopy (HRTEM), and first-principles calculations. Furthermore, two correspondent phase transitions and metallization for Sb_2S_3 were discussed in detail at high pressure.

II. EXPERIMENTAL AND COMPUTATIONAL DETAILS

Commercially available 99.999% Sb_2S_3 powder was purchased from Alfa-Aesar. High-pressure Raman spectroscopy experiments were conducted using a DAC with an anvil culet of 300 μm. Ruby single crystal with a grain size of $\sim$5 μm was used for pressure calibration on the basis of the wave-number shift of the fluorescence band of the trivalent chromic ion. Helium was used as the pressure medium to provide a hydrostatic condition, and no pressure medium was used for the nonhydrostatic condition. Raman spectra were collected using a Raman spectrometer (Invia, Renishaw) equipped with a confocal microscope (TCS SP8, Leica) and a CCD camera (Olympus). The typical excitation laser power was $\sim$20 mW for Raman spectroscopy and 0.5–40 μW for fluorescence spectroscopy. Spectra were taken for the backscattering geometry using an argon ion laser (Spectra physics; 514.5 nm and power $<$1 mW) in the range $100-500$ cm^{-1} with a spectral resolution of 1.0 cm^{-1}. Each spectrum was acquired during 480 s, and we waited 15 min after each increase for pressure stabilization. Raman spectra were fitted by a Lorenz-type function using PEAKFIT software to determine the positions of the Raman modes. All of these observations on the atomic force microscopy (AFM) and transmission electron microscopy (TEM) images were obtained using a Multimode 8 mass spectrometer (Bruker) and Tecnai G2 F20 S-TWIN TMP, respectively.

High-pressure electrical conductivity experiments were conducted in a DAC with a 300-μm-diam anvil culet. The sample was crushed into a powder ($\sim$20 μm). A rhenium gasket was preindented to a thickness of $\sim$60 μm and a 180-μm hole was drilled with a laser. Then, a mixture of boron nitride powder and epoxy was compressed into the hole, and another 100-μm hole was drilled as an insulating sample chamber. A cross-sectional assembly of the designed DAC used in this study is shown in Fig. 1. ac impedance spectroscopy was performed with the Solartron-1260 and Solartron-1296 impedance spectroscopy analyzers in the frequency range $10^{-1}-10^{7}$ Hz. A plate electrode was integrated between two

symmetric diamond anvils [18]. The temperature was monitored with a k-type thermocouple with an estimated accuracy of 5 K. Detailed descriptions of the high-pressure equipment and experimental procedures can be found elsewhere [19–22].

Density-functional theory and the pseudopotential method were applied for the first-principles calculations, and the electronic structure was performed using the CASTEP code. The exchange and correlation terms were obtained in the generalized gradient approximation (GGA) with the Perdew-Burke-Ernzerhof scheme. Structural optimizations were conducted using the Broyden-Fletcher-Goldfarb-Shanno minimization algorithm provided in this code. Integration of the Brillouin zone was carried out using the special k points generated by $2 \times 6 \times 2$ parameter grids for the *Pnma* phases to ensure high convergence of 1–2 meV per atom in the total energy. One electronic valence state was expanded on the basis of a plane wave with a cutoff energy of 450 eV. Structural parameters including the atomic positional coordinates, bond lengths, and bond angles for Sb_2S_3 are obtained from previous study after being optimized [23].

III. RESULTS AND DISSCUSSION

Raman spectroscopy is a sensitive probe for detecting isostructural transitions at high pressure [8–10]. In Fig. 2, the Raman spectra of Sb_2S_3 are shown at room temperature up to $\sim$40 GPa. Below 5.0 GPa, five typical Raman vibration modes are observed, which are attributed as follows: the peaks at 189 cm^{-1} (A_g^6) and 240 cm^{-1} (B_{1g}^5) corresponded to the antisymmetric S-Sb-S and symmetric bending modes, respectively [24]; the peaks at 300 cm^{-1} (B_{2g}^{10}) and 283 cm^{-1} (A_g^9) corresponded to antisymmetric Sb-S stretching vibrations; and the peak at 310 cm^{-1} (B_{2g}^9) is generated by the symmetric stretching vibration [24]. Five representative vibrations are attributed to the trigonal pyramidal four-atom groups Sb_1S_3 [24]. The pressure dependences of Raman modes for Sb_2S_3 and the obtained fitting results are displayed in Fig. 2 and Table I, respectively.

Under a nonhydrostatic condition [Figs. 2(a) and 2(b)], we obtained two positive $\partial\omega/\partial P$ values (ω and P are the assumed Raman shift and pressure, respectively) from 2.12 to 2.31 cm^{-1}GPa^{-1} at Raman shifts below 250 cm^{-1} (corresponding to A_g^6 and B_{1g}^5 modes, respectively), and three negative $\partial\omega/\partial P$ values (corresponding to A_g^9, B_{2g}^{10}, and B_{2g}^9
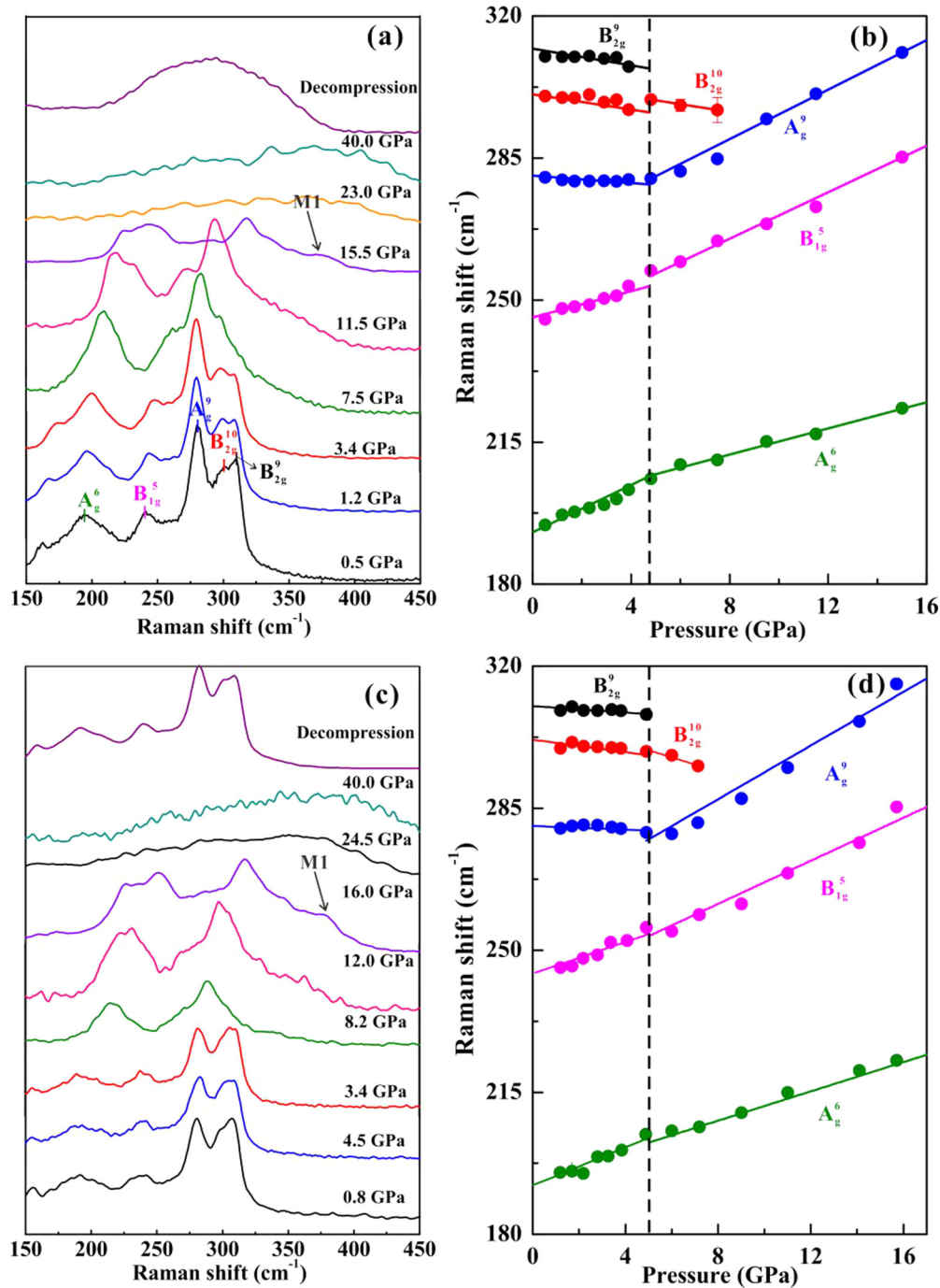
FIG. 2. Raman spectroscopic results of Sb_2S_3 at high pressure. (a), (c) Raman spectra at each representative pressure point ($\lambda = 514$ nm and $T = 300$ K). (b), (d) Raman mode frequency evolution against pressure for Sb_2S_3 in nonhydrostatic and hydrostatic conditions, respectively. A new low-intensity Raman mode appears at about ~ 15 GPa (denoted as M1). Errors in both frequency and pressure are within the size of the symbol.

modes, respectively) from -0.20 to -0.79 cm^{-1} GPa^{-1} at Raman shifts above 250 cm^{-1} and pressures below 5.0 GPa. Above 5.0 GPa, we obtained three positive $\partial\omega/\partial P$ values (corresponding to A_g^6, B_{1g}^5, and A_g^9 modes, respectively) from 1.65 to 3.25 cm^{-1}GPa^{-1} at Raman shifts below 290 cm^{-1}, and one negative $\partial\omega/\partial P$ value (corresponding to the B_{2g}^{10} mode) of -0.92 cm^{-1} GPa^{-1} at a Raman shift above 290 cm^{-1}.

Under a hydrostatic condition, we obtained two positive $\partial\omega/\partial P$ values of 2.84 and 2.48 cm^{-1}GPa^{-1} at Raman shifts below 250 cm^{-1}, and three negative $\partial\omega/\partial P$ values of -0.32, -0.71, and -0.70 cm^{-1}GPa^{-1} at Raman shifts above 250 cm^{-1} at pressures below 5.0 GPa. Above 5.0 GPa, we obtained three positive $\partial\omega/\partial P$ values of 1.95, 2.91, and 3.56 cm^{-1}GPa^{-1} at Raman shifts below 290 cm^{-1}, and one negative $\partial\omega/\partial P$

TABLE I. Pressure dependence of the Raman shift for Sb_2S_3 under nonhydrostatic and hydrostatic conditions.

Pressure condition	Mode	$\omega(P_0)(cm^{-1})$	$\partial\omega/\partial P(cm^{-1}GPa^{-1}) < 5.0\,GPa$	$\partial\omega/\partial P(cm^{-1}GPa^{-1}) > 5.0\,GPa$
Nonhydrostatic	A_g^6	189.0	2.31	1.65
	B_{1g}^5	240.0	2.12	2.64
	A_g^9	283.0	−0.20	3.25
	B_{2g}^{10}	299.2	−0.79	−0.92
	B_{2g}^9	310.0	−0.76	
Hydrostatic	A_g^6	189.0	2.84	1.95
	B_{1g}^5	240.0	2.48	2.91
	A_g^9	283.0	−0.32	3.56
	B_{2g}^{10}	299.2	−0.71	−1.50
	B_{2g}^9	310.0	−0.70	

value of $-1.50\,cm^{-1}GPa^{-1}$ at a Raman shift above $290\,cm^{-1}$.

We also observed the vanishing of the B_{2g}^9 mode under nonhydrostatic and hydrostatic conditions above ~5 GPa. An obvious discontinuity at ~5 GPa characterized by the pressure dependence of Raman modes is consistent with previously reported results, and it is strong evidence for an IPT [16]. In addition, we also found a new low-intensity Raman mode at about ~15 GPa (denoted as M1 in Fig. 2), suggesting that the compound may have undergone a new pressure-induced phase transition [1,16]. When the pressure is increased to ~23.0 GPa the Raman modes exhibit pronounced broadening, becoming featureless. Upon further compression to 40.0 GPa a single amorphous state is observed, which is consistent with the high-pressure synchrotron x-ray diffraction results reported by Efthimiopoulos *et al.* [16].

Previous reports of the pressure-induced phase transition for Sb_2S_3 at room temperature are inconsistent [5,15,16]. For example, Efthimiopoulos *et al.* [16] reported an ~5 GPa phase transition on the basis of the evolution of the Raman-active modes and lattice parameter axial ratios, which may reflect an ETT. Similarly, Sorb *et al.* [15] observed an ~4 GPa phase transition using Raman spectroscopy. However, according to Raman scattering and XRD data and theoretical calculations, Ibáñez *et al.* [5] concluded that there was no evidence for a second-order IPT or ETT in Sb_2S_3 at high pressure. In the present work, our Raman spectroscopy results provide robust evidence for an IPT at ~5.0 GPa, in which a strong phonon-phonon interaction is generated [16]. Although previous high-pressure XRD results did not reveal a first-order phase transition up to ~25 GPa, the discontinuous change of the parameter axial ratio is indicative of an IPT [5], which is well documented for similar structural compounds in A_2B_3 series [8–10].

As shown in Fig. 2, the changes in the Raman spectra upon decompression from 40.0 GPa were irreversible under a nonhydrostatic condition. However, for a hydrostatic condition, one reversible characteristic was observed upon decompression. This may be attributed to one or both of the following two factors: (i) high pressure is necessary to break the thermodynamic stability of the lattice structure, which will restrain the recovery of the stable crystalline phase and result in irreversible amorphization; (ii) deviatoric stress under

a nonhydrostatic condition will facilitate the transformation of long-range order to long-range correlated disorder in the lattice. As a matter of fact, the irreversible amorphization also occurred in other material (α-As_2Te_3) in the nonhydrostatic condition due to the irreversible lattice distortion [25].

Structural transitions and IPTs are often accompanied by an electronic phase transition. The decrease in the distance of atoms within and between layers in Sb_2S_3 is expected to modulate the electronic properties [26]. To confirm the IPT and other changes in the electrical properties of Sb_2S_3, pressure-induced electrical conductivity measurements were carried out up to 40.1 GPa. Representative Nyquist plots for Sb_2S_3 are shown in Figs. 3(a)–3(c) in the pressure range of 1.7–40.1 GPa. With increasing pressure, the grain boundary effect of the sample gradually becomes weaker. When the pressure is higher than 17.8 GPa, only one grain interior impedance arc is observed in the fourth quadrant. Figure 3(d) shows the pressure-dependent logarithm of the electrical conductivity of Sb_2S_3 in the process of compression and decompression at room temperature. The electrical conductivity decreases with increasing pressure up to 5.2 GPa, and then remains relatively constant in the range of 5.2–15.0 GPa. From 15.0 to 33.3 GPa, the electrical conductivity drastically increases before stabilizing above 33.3 GPa. Thus, four discrete pressure ranges can be identified by variation in the slope of pressure versus conductivity: from ambient pressure to 5.2 GPa, 5.2 to 15.0 GPa, 15.0 to 33.3 GPa, and 33.3 to 40.1 GPa, which correspond to rates of -0.069, 0.0003, 0.21, and $0.011\,S\,cm^{-1}GPa^{-1}$, respectively. Although no evidence has been found in previous studies for symmetric changes and volume discontinuities [5,16], the variation of conductivity and Raman modes for Sb_2S_3 at ~5.0 GPa may be attributed to a secondary IPT. The sharp increase in conductivity between 15.0 and 33.3 GPa [Fig. 3(d)] can be ascribed to the increasing overlap of the electronic orbital wave function and the narrowing energy gap. The abrupt variation of the electrical conductivity at ~15.0 GPa may be attributed to a pressure-induced phase transition, which is in good agreement with our obtained results from Raman spectroscopy data. From 33.3 to 40.1 GPa, the conductivity is relatively constant at $\sim7.2\,S\,cm^{-1}$, and such high electrical conductivity may be indicative of metallization. Interestingly, after the pressure was decreased to atmospheric pressure, the electrical conductivity decreased to $\sim0.5\,S\,cm^{-1}$,
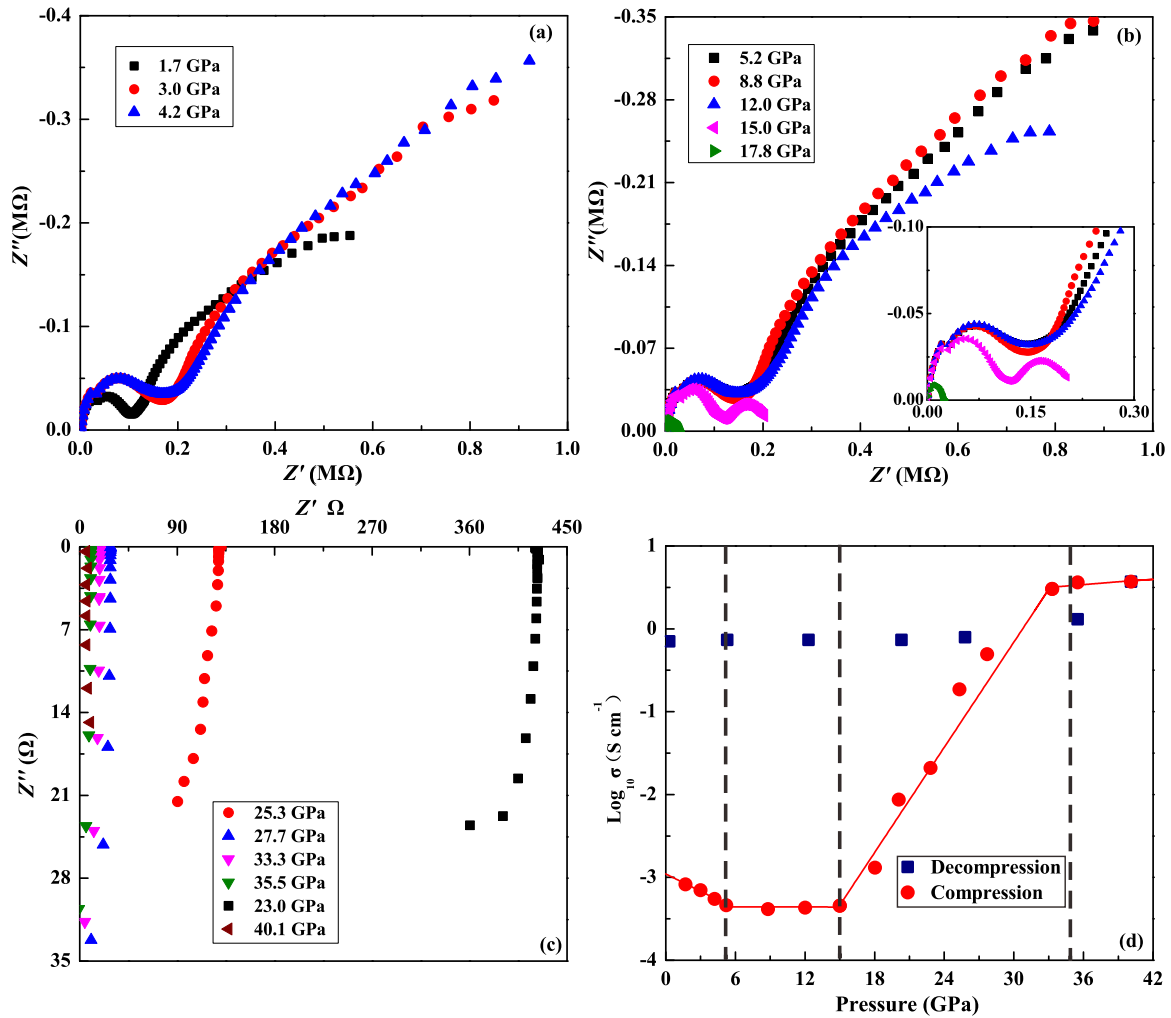
FIG. 3. (a)–(c) Nyquist plots of impedance spectra for Sb_2S_3 at different pressures. (d) Pressure-dependent electrical conductivity of Sb_2S_3 in the process of compression and decompression.

where it remained for an extended period (i.e., 100 h). The irreversible metallization phenomenon is a peculiar property of many layered materials, as we have reported for molybdenum disulfide, which has a similar layered structure to Sb_2S_3 [27].

To verify whether Sb_2S_3 undergoes pressure-induced irreversible metallization, we conducted a series of high-pressure variable-temperature conductivity measurements. The electrical conductivity and temperature for Sb_2S_3 were found to satisfy the Arrhenius relation, as shown in Fig. 4. Below 34.0 GPa, the electrical conductivity increased with increasing temperature, indicating that Sb_2S_3 is a semiconductor under these conditions. Above 34.0 GPa, the electrical conductivity decreased with temperature, a clear indication of pressure-induced metallization. It is well known that Sb_2S_3 and Sb_2Se_3 have almost identical electronic band structures and that Sb_2Se_3 becomes metallic when compressed to ∼3.5 GPa [13]. The mechanism for metallization differs markedly between the two materials, as is evident from the behavior of the Sb^{3+} lone-electron pair (LEP) after the IPT: in Sb_2Se_3, there is almost complete s-p orbital hybridization of the Sb^{3+} LEP; by contrast, at pressures up to 10 GPa in Sb_2S_3, the Sb^{3+} LEP does not hybridize strongly with its neighboring s-p orbitals [16]. The lack of LEP hybridization with s-p

orbitals in Sb_2S_3 is the reason why an insulator-metal transition is observed for Sb_2S_3 at such high pressure (∼34.0 GPa). Therefore, we can attribute the metallization to the sufficiently small LEP activity, which results in a strong hybridization between LEP and its neighboring s-p orbitals. In addition, it can be seen from Fig. 4(d) that Sb_2S_3 also exhibited a typical metallic behavior after decompression to ambient pressure, which is also consistent with our previously reported results for molybdenum disulfide [27].

Figure 5(a) shows the relationship among pressure, temperature, and electrical conductivity. It clearly indicates a pressure-induced phase transition from semiconductor to metal for Sb_2S_3. According to the temperature dependence of the conductivity, the transport activation energy of Sb_2S_3 at a given pressure can be obtained from

$$\sigma = \sigma_0 \exp(-E_t/k_B T), \qquad (1)$$

where σ_0 is the preexponential factor (S m^{-1}), E_t is the transport activation energy (eV), k_B is the Boltzmann constant, and T is the absolute temperature (K). The value of E_t can be obtained by linearly fitting the logarithmic conductivity as a function of $1000/T$. The effect of pressure on the activation energy for Sb_2S_3 is shown in Fig. 5(b). With increasing
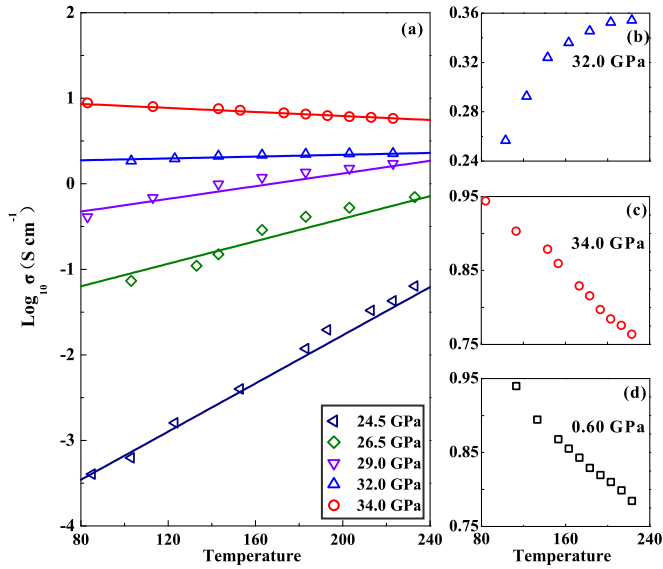
FIG. 4. (a) The pressure dependence of conductivity for Sb_2S_3 as a function of temperature, with the maximum pressure up to 34.0 GPa. (b), (c) The conductivity curves of Sb_2S_3 as a function of temperature at representative pressures: 32.0 and 34.0 GPa, respectively. (d) The metallic state of Sb_2S_3 after decompression to 0.6 GPa.

pressure, the activation energy decreases, making it easier for charge carriers to jump across the potential barrier. The value of E_t approaches zero when the pressure is increased to ~32.0 GPa, which implies that the typical semiconductor behavior and energy barrier disappear at this pressure. In other words, Sb_2S_3 exhibits a metallic conduction behavior above 32.0 GPa.

To reveal the structural transformation of Sb_2S_3 after metallization, the recovered samples were analyzed using HRTEM and AFM (Fig. 6). The HRTEM images revealed an original interlayer spacing of ~0.4 nm [Fig. 6(a), inset]. After decompression from 35.0 GPa, the sample transformed to an amorphous state with an ~0.17 nm interlayer spacing in the residual layered structure under a nonhydrostatic condition

[Fig. 6(a)]. However, the layered structure of Sb_2S_3 was perfectly preserved upon decompression from 36.5 GPa under a hydrostatic condition [Fig. 6(c)]. This means that the reduction in interlayer spacing and amorphization was irreversible under a nonhydrostatic condition. However, the molecules of the pressure medium entered the interlayer spacing and weakened the interlayer interactions, which caused the change in spacing to be reversible and protected the layered structure for Sb_2S_3 under a hydrostatic condition. As seen in Fig. 6(b), the surface morphology after decompression from 35.0 GPa was lumpy and had significantly compacted as a result of the lack of protection of a pressure medium. In contrast, the layered structure of Sb_2S_3 under a hydrostatic condition was well preserved upon decompression from 36.5 GPa [Fig. 6(d)]. Previous studies have reported the transformation from semiconductor to metal for other two-dimensional materials [27]. In general, the change of electronic structure and the closure of the band gap are accompanied by a structural phase transition in these layered materials, which is reversible upon decompression. However, certain pressures will induce irreversible phase transitions. In the future, the unique, pressure-dependent electronic structure of layered materials may be used for band-gap tuning of semiconductor devices.

Theoretical predictions of the band structure, total density, and projected density for Sb_2S_3 are presented in Fig. 7 at different pressures. These results predict that Sb_2S_3 has a theoretical quasidirect fundamental band gap of 1.28 eV at ambient pressure, which is consistent with the results of a previous study [5]. The band gap is 0.07 eV at 30.0 GPa and it is closed at 40.0 GPa, which indicates that the material has undergone a semiconductor-to-metal transition. These results agree well with our experimental data, providing further evidence for metallization of Sb_2S_3 at around 34.0 GPa. As shown in Fig. 7, the lowest valence bands (between about -14 and -12 eV) are dominated by S 3s states; the valence bands (between about -10 and -7 eV) are mainly managed by Sb 5s states. The highest occupied valence bands are dominated by S 3p states. Above the Fermi level, the conduction band is composed of S 3s, S 3p, Sb 5s, and Sb 5p states mutually hybridized and dominated by Sb 5p. The electronic coupling and hybridization
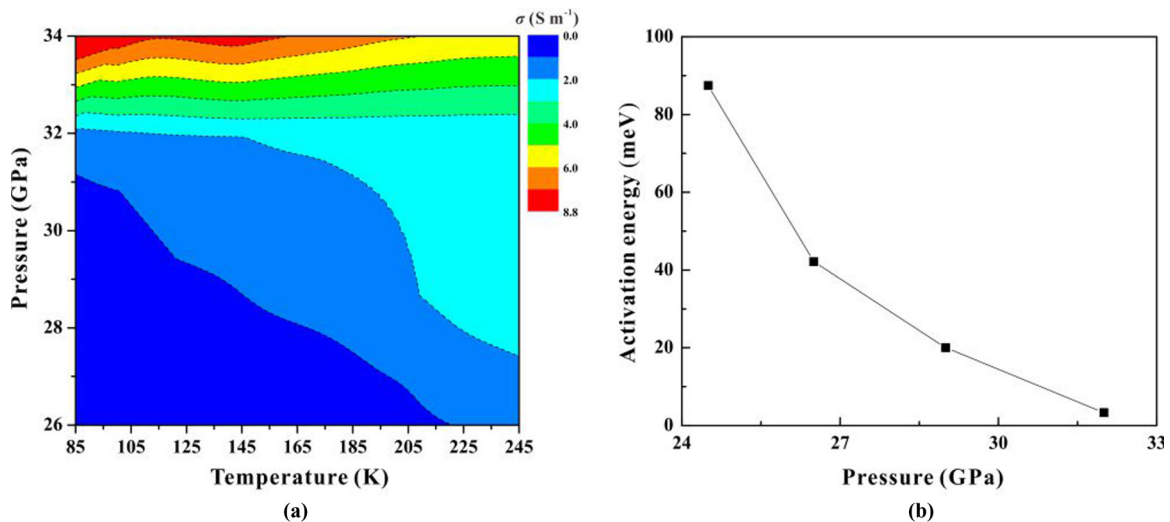

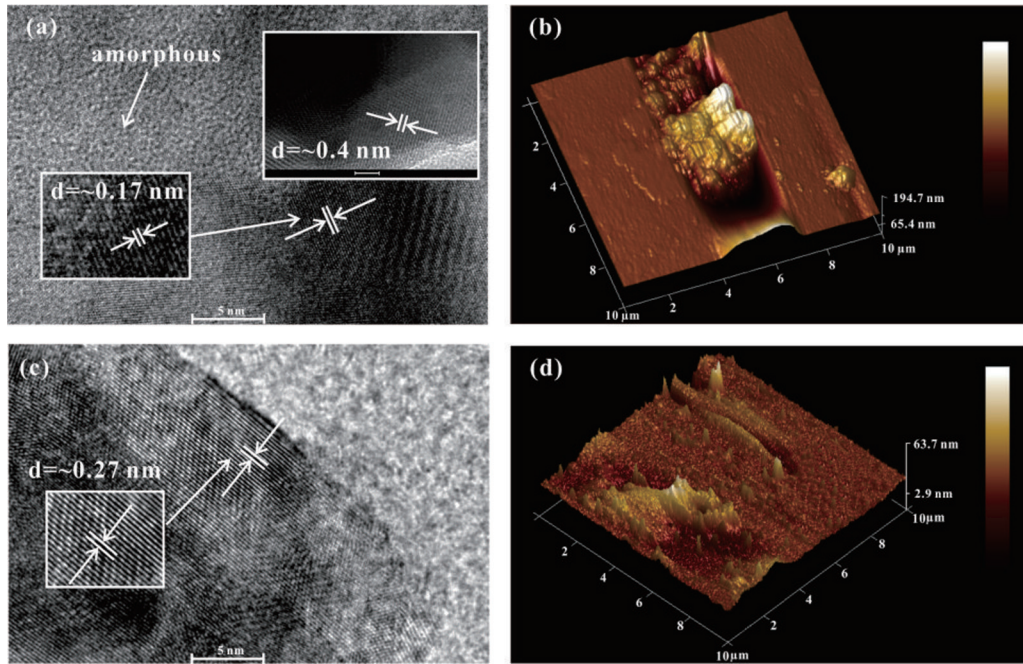FIG. 5. (a) Temperature-pressure-conductivity contour map. (b) Pressure dependence of activation energy for Sb_2S_3.

FIG. 6. (a), (c) HRTEM images of decompressed Sb_2S_3 from 35.0 GPa under a nonhydrostatic condition and 36.5 GPa under a hydrostatic condition, respectively. Inset: HRTEM image of the initial sample. Scale bars are 5 nm. (b), (d) AFM image of pressure-induced morphology of decompressed Sb_2S_3 from 35.0 GPa under a nonhydrostatic condition and 36.5 GPa under a hydrostatic condition, respectively.

become more and more intensive with increasing pressure, which leads to the diffusion of the valence and conduction bands; this is particularly pronounced for the high-energy valence bands. The conduction bands widen slightly, which results in a decrease in the band gap and a dramatic increase in the electrical conductivity for Sb_3S_2 at pressures above 15.0 GPa.
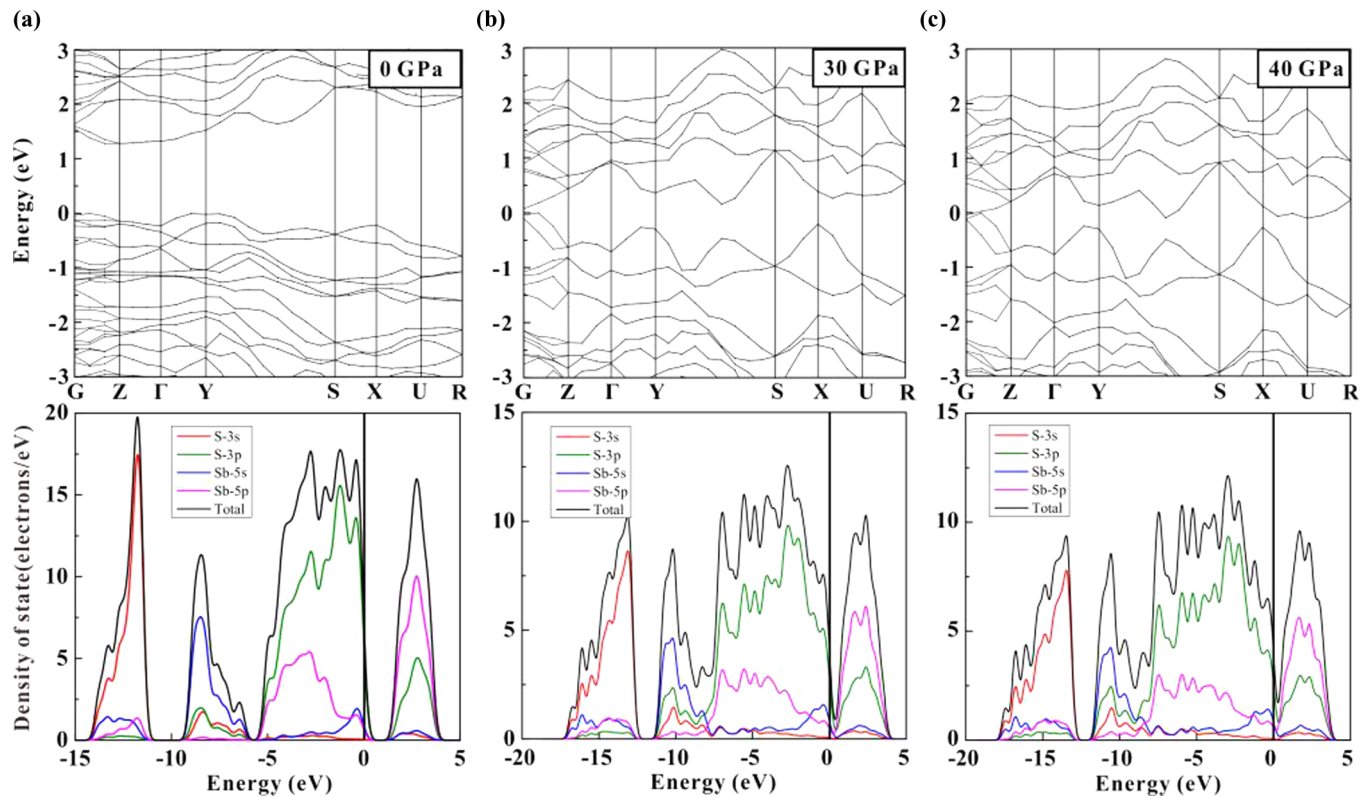

FIG. 7. Calculated band structure, total density, and projected density for Sb_2S_3 at 0, 30.0, and 40.0 GPa. The band gaps for (a) and (b) are 1.28 and 0.07 eV, respectively. The band gap for (c) has already closed. The band gap of Sb_2S_3 narrows with increasing pressure.

IV. CONCLUSIONS

The structural, vibrational, and electronic properties of Sb_2S_3 up to ∼40.1 GPa were determined using a diamond anvil cell in conjunction with ac impedance spectroscopy, Raman spectra, AFM, HRTEM, and theoretical calculations. From the temperature-dependent conductivity measurements and theoretical calculations, a semiconductor-to-metal transition was found at ∼34.0 GPa. The AFM and HRTEM images for the recovered (i.e., decompressed) sample confirmed that the reduction in interlayer spacing was irreversible because of a strongly deviatoric stress. On the basis of the noticeable changes in the Raman-active modes and a variation in the slope of the conductivity, an IPT and pressure-induced phase transition were revealed at ∼5.0 and ∼15.0 GPa, respectively. The high-pressure properties obtained for Sb_2S_3 will be helpful to understand the crystal structure evolution and electrical characteristics of A_2B_3-type compounds, facilitating their application in electronic devices.

[1] A. Efstathiou and E. R. Levin, J. Opt. Soc. Am. **58**, 373 (1968).

[2] S. J. Moon, Y. Itzhaik, J. H. Yum, S. M. Zakeeruddin, G. Hodes, and M. Grätzel, J. Phys. Chem. Lett. **1**, 1524 (2010).

[3] M. R. Filip, C. E. Patrick, and F. Giustino, Phys. Rev. B **87**, 205125 (2013).

[4] P. Bayliss and W. Nowacki, Z. Krist-Cryst. Mater. **135**, 308 (1972).

[5] J. Ibáñez, J. A. Sans, Popescu, C. J. López-Vidrier, J. J. Elvira-Betanzos, V. P. Cuenca-Gotor, O. Gomis, F. J. Manjón, P. Rodríguez-Hernández, and A. Muñoz, J. Phys. Chem. C **120**, 10547 (2016).

[6] T. Ben Nasr, H. Maghraoui-Meherzi, and N. Kamoun-Turki, J. Alloys Compd. **663**, 123 (2016).

[7] R. G. S. Marquina, T. G. Sanchez, N. R. Mathews, and X. Mathew, Mater. Res. Bull. **90**, 285 (2017).

[8] R. Vilaplana, O. Gomis, F. J. Manjón, A. Segura, E. Pérez-González, P. Rodríguez-Hernández, A. Muñoz, J. González, V. Marín-Borrás, V. Muñoz-Sanjosé, C. Drasar, and V. Kucek, Phys. Rev. B **84**, 104112 (2011).

[9] R. Vilaplana, D. Santamaría-Pérez, O. Gomis, F. J. Manjón, J. González, A. Segura, A. Muñoz, P. Rodríguez-Hernández, E. Pérez-González, V. Marín-Borrás, V. Muñoz-Sanjose, C. Drasar, and V. Kucek, Phys. Rev. B **84**, 184110 (2011).

[10] O. Gomis, R. Vilaplana, F. J. Manjón, P. Rodríguez-Hernández, E. Pérez-González, A. Muñoz, V. Kucek, and C. Drasar, Phys. Rev. B **84**, 174305 (2011).

[11] I. Efthimiopoulos, J. Kemichick, X. Zhou, S. V. Khare, D. Ikuta, and Y. Wang, J. Phys. Chem. A **118**, 1713 (2014).

[12] A. Polian, M. Gauthier, S. M. Souza, D. M. Trichês, J. Cardoso de Lima, and T. A. Grandi, Phys. Rev. B **83**, 113106 (2011).

[13] P. P. Kong, F. Sun, L. Y. Xing, J. Zhu, S. J. Zhang, W. M. Li, Q. Q. Liu, X. C. Wang, S. M. Feng, X. H. Yu, J. L. Zhu, R. C. Yu, W. G. Yang, G. Y. Shen, Y. S. Zhao, R. Ahuja, H. K. Mao, and C. Q. Jin, Sci. Rep. **4**, 6679 (2014).

[14] J. L. Zhang, S. J. Zhang, H. M. Weng, W. Zhang, L. X. Yang, Q. Q. Liu, S. M. Feng, X. C. Wang, R. C. Yu, L. Z. Cao, L. Wang, W. G. Yang, H. Z. Liu, W. Y. Zhao, S. C. Zhang, X. Dai, Z. Fang, and C. Q. Jin, Proc. Natl. Acad. Sci. (USA) **108**, 24 (2011).

[15] Y. A. Sorb, V. Rajaji, P. S. Malavi, U. Subbarao, P. Halappa, S. C. Peter, S. Karmakar, and C. Narayana, J. Phys.: Condens. Matter **28**, 015602 (2016).

[16] I. Efthimiopoulos, C. Buchan, and Y. Wang, Sci. Rep. **6**, 24246 (2016).

[17] L. F. Lundegaard, R. Miletich, T. Balic-Zunic, and E. Makovicky, Phys. Chem. Miner. **30**, 463 (2003).

[18] M. Li, C. X. Gao, Y. Z. Ma, Y. C. Li, X. D. Li, H. Li, J. Liu, A. M. Hao, C. Y. He, X. W. Huang, D. M. Zhang, and C. L. Yu, Rev. Sci. Instrum. **77**, 123902 (2006).

[19] L. D. Dai, L. Wu, H. P. Li, H. Y. Hu, Y. K. Zhuang, and K. X. Liu, J. Phys.: Condens. Matter **28**, 475501 (2016).

[20] L. D. Dai, L. Wu, H. P. Li, H. Y. Hu, Y. K. Zhuang, and K. X. Liu, Europhys. Lett. **114**, 56003 (2016).

[21] L. Wu, L. D. Dai, H. P. Li, Y. K. Zhuang, and K. X. Liu, J. Phys. D **49**, 345102 (2016).

[22] L. Wu, L. D. Dai, H. P. Li, H. Y. Hu, Y. K. Zhuang, and K. X. Liu, J. Appl. Phys. **121**, 125901 (2017).

[23] A. Kyono and K. M.imata, Am. Mineral. **89**, 932 (2004).

[24] S. Kharbish, E. Libowitzky, and A. Beran, Eur. J. Mineral. **21**, 325 (2009).

[25] L. D. Dai, Y. K. Zhuang, H. P. Li, L. Wu, H. Y. Hu, K. X. Liu, L. F. Yang, and C. Pu, J. Mater. Chem. C **5**, 12157 (2017).

[26] C. Y. Li, J. G. Zhao, Q. Y. Hu, Z. G. Liu, Z. H. Yu, and H. Yan, J. Alloys Compd. **688**, 329 (2016).

[27] Y. K. Zhuang, L. D. Dai, L. Wu, H. P. Li, H. Y. Hu, K. X. Liu, L. F. Yang, and C Pu, Appl. Phys. Lett. **110**, 122103 (2017).